Heliyon 9 (2023) e17200

Contents lists available at ScienceDirect

Heliyon

journal homepage: www.cell.com/heliyon

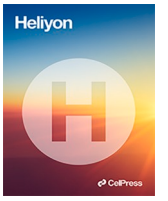

RGO decorated N-doped $NiCo_2O_4$ hollow microspheres onto activated carbon cloth for high-performance non-enzymatic electrochemical glucose detection

Prashant Shivaji Shewale, Kwang-Seok Yun *

Department of Electronic Engineering, Sogang University, Seoul, Republic of Korea

ARTICLE INFO

Keywords:
$NiCo_2O_4$
RGO
Composite
N-doping
Non-enzymatic
Glucose detection

ABSTRACT

This paper reports the first effective fabrication of a high-performance non-enzymatic glucose sensor based on activated carbon cloth (ACC) coated with reduced graphene oxide (RGO) decorated N-doped urchin-like nickel cobaltite ($NiCo_2O_4$) hollow microspheres. Hierarchically mesoporous N-doped $NiCo_2O_4$ hollow microspheres were synthesized using a facile solvothermal method, followed by thermal treatment in a nitrogen (N_2) atmosphere. Subsequently, they were hydrothermally decorated with RGO nanoflakes. The resulting composite was dip-coated onto ACC, and its electrochemical and glucose sensing performances were investigated using electrochemical impedance spectroscopy (EIS), cyclic voltammetry (CV), and chronoamperometric measurements in a three-electrode system. The composite electrode sensor demonstrates admirable sensitivity (6122 $\mu M\ mM^{-1}\ cm^{-2}$) with an ultralow detection limit (5 nM, S/N = 3), and it performs well within a substantial linear range (0.5–1.450 mM). Additionally, it exhibits good long-term response stability and outstanding anti-interference performance. These outstanding results can be attributed to the synergistic effects of the highly electrically conductive ACC with multiple channels, the enhanced catalytic activity of highly porous N-doped $NiCo_2O_4$ hollow microspheres, and the large electroactive sites provided by its well-developed hierarchical nanostructure and RGO nanoflakes. The findings highlight the enormous potential of the ACC/N-doped $NiCo_2O_4$@RGO electrode for non-enzymatic glucose sensing.

1. Introduction

In the microenvironment of the human body, glucose plays a vital role as a nutrient directly involved in metabolic processes. However, elevated glucose levels can be detrimental to health, leading to conditions such as diabetes mellitus. If left uncontrolled, diabetes mellitus can pose significant risks to physical well-being and even result in fatality [1]. Consequently, accurately identifying the concentration of glucose in the blood is crucial for the diagnosis, treatment, and management of diabetes mellitus. Although traditional enzymatic glucose sensors exhibit high sensitivity and selectivity, their costliness and susceptibility to pH, temperature, and humidity constraints limit their further development [2]. As a result, non-enzymatic electrochemical glucose biosensors have garnered considerable attention in current research efforts [3–9].

With the advancements in nanotechnology, several non-enzymatic glucose electrodes based on transition metal oxides and other

* Corresponding author.
E-mail address: ksyun@sogang.ac.kr (K.-S. Yun).

https://doi.org/10.1016/j.heliyon.2023.e17200
Received 1 March 2023; Received in revised form 7 June 2023; Accepted 9 June 2023
Available online 12 June 2023

composite materials have been developed [10–21]. Among them, spinel $NiCo_2O_4$ has garnered significant interest due to its high natural abundance, low cost, non-toxicity, and environmental friendliness [22]. Additionally, the interphases of nickel (Ni) and cobalt (Co) in the spinel structure exhibit strong electrical interactions, thereby enhancing the electrocatalytic activity and chemical stability of the electrode material. However, $NiCo_2O_4$ also has certain limitations, such as low electrical conductivity and poor chemical/mechanical stability [23]. Therefore, there is an opportunity to enhance the glucose-sensing characteristics of $NiCo_2O_4$, and various approaches have been explored thus far. One such approach involves synthesizing $NiCo_2O_4$ in various morphologies to improve its electrochemical performance, as the surface morphology significantly affects ion transport kinetics and electrolyte permeation. In particular, hierarchical hollow nanostructures of $NiCo_2O_4$ have been found to significantly enhance performance in electrochemical applications. This is attributed to their large specific surface area, short diffusion routes for ions or electrons, and efficient mass transport channels [24].

Furthermore, the combination of porous carbon materials like RGO with $NiCo_2O_4$ has been found to enhance the electrode material's conductivity, active sites, specific surface area, and therefore its glucose sensing properties [25,26]. Additionally, doping metal oxides with heteroatom elements such as N, P, and S can increase their electrical conductivity while enhancing the intrinsic activity at each site [27,28]. Notably, the lone-pair electrons around N atoms can improve the interaction with the metal atoms, and the resulting M-O-N bonds exhibit increased electronegativity and elongated bond lengths. This reduces the attraction of $Co^{2+}/Co^{3+}/Ni^{2+}/Ni^{3+}$ to the 3d electrons and decreases the electron transport energy, thereby improving the reaction kinetics [29,30]. Interestingly, in the metallic oxide lattice, doping N atoms partially replace intrinsic O atoms, leading to the introduction of a significant number of oxygen defects. These defects can effectively alter the electronic structure and chemical properties of crystalline materials, as well as their electrical conductivity, by causing slight atom-to-atom disruptions and lattice deformation [31]. The synergistic effects of large multivalent metal cations and oxygen vacancies have been proven to considerably enhance the electronic conductivity and electrochemical performance of electrodes [23]. Therefore, it is crucial to consider a plausible design that incorporates doping, defects, and surface-structural engineering to improve the electrochemical characteristics and overall performance of glucose-sensing electrodes. Consequently, research focusing on high-performance glucose sensors based on activated carbon cloth coated with N-doped $NiCo_2O_4$ urchin-like hollow microspheres decorated with RGO nanoflakes appears necessary and has been scarcely mentioned in previous publications.

In this study, we have successfully fabricated a high-performance glucose sensor based on N-doped $NiCo_2O_4$@RGO composite-coated activated carbon cloth (ACC). The glucose sensor exhibits superior electrochemical performance attributed to several key factors. Firstly, the highly mesoporous structure of the composite provides a large surface area, allowing for enhanced glucose sensing capabilities. Secondly, the N-doping in $NiCo_2O_4$ increases the number of catalytic active sites, leading to improved electrochemical activity. Moreover, the N-doping also contributes to the modification of the electronic structure and enhancement of electrical conductivity in $NiCo_2O_4$. These combined effects contribute to the glucose sensor's excellent performance, including high glucose sensitivity with a very low detection limit, remarkable stability, wide detection range, and rapid response time. Furthermore, the glucose sensor exhibits exceptional selectivity for glucose compared to the majority of the primary interfering species commonly found in human serum. This selectivity ensures accurate and reliable glucose detection in complex biological samples. Overall, our findings demonstrate the significant potential of the N-doped $NiCo_2O_4$@RGO composite-coated ACC glucose sensor, highlighting its excellent electrochemical performance and promising application in glucose sensing.

2. Experimental details

2.1. Synthesis of N-doped -$NiCo_2O_4$@RGO urchin-like hollow microspheres

We employed a simple solvothermal technique to prepare $NiCo_2O_4$ hollow microsphere precursors. In this process, urea (10.8 g), cobalt (1.74 g), and nickel (0.87 g) nitrates were added to a solution consisting of 45 ml of isopropyl alcohol (IPA) and 9 ml of deionized water. The mixture was continuously stirred until the complete dissolution of the compounds. Subsequently, the resulting solution was transferred to a stainless steel autoclave and subjected to constant stirring for 1 h. The autoclave was then placed in an electric oven and maintained at 120 °C for 12 h during the solvothermal reaction. After completion, the autoclave was gradually cooled to room temperature. To purify the precipitates, they were retrieved from the Teflon container, transferred to conical tubes, and underwent five cycles of centrifugation using deionized water and ethyl alcohol. Subsequently, the cleaned powder slurries were dried at 80 °C for 12 h and then calcined at 350 °C for 2 h to obtain black urchin-like $NiCo_2O_4$ hollow microspheres (referred to as HN).

For the preparation of N-doped $NiCo_2O_4$ hollow microspheres, namely N_{50}–HN, N_{100}–HN, and N_{150}–HN, a similar procedure was followed. However, the $NiCo_2O_4$ powder samples were calcined in a vacuum tube furnace with a continuous flow of pure nitrogen gas at flow rates of 50, 100, and 150 standard cubic centimeters per minute (sccm), respectively. The calcination was carried out at a temperature of 300 °C for 2 h [32]. The obtained microspheres were then immersed in a homogeneous aqueous solution containing urea and graphene oxide (GO) in a ratio of 15:1. This mixture was placed in an autoclave vessel, and a hydrothermal reaction was conducted at 120 °C for 8 h to synthesize RGO-decorated HN, N_{50}–HN, N_{100}–HN, and N_{150}–HN microspheres, denoted as HN@R, N_{50}–HN@R, N_{100}–HN@R, and N_{150}–HN@R, respectively. Subsequently, the microspheres underwent a second drying process at 80 °C for 12 h.

2.2. Deposition of N-doped-$NiCo_2O_4$@RGO composites on ACC

To prepare the ACC/HN@R and ACC/N_{100}–HN@R electrodes, the HN@R and N_{100}–HN@R microspheres, along with a small

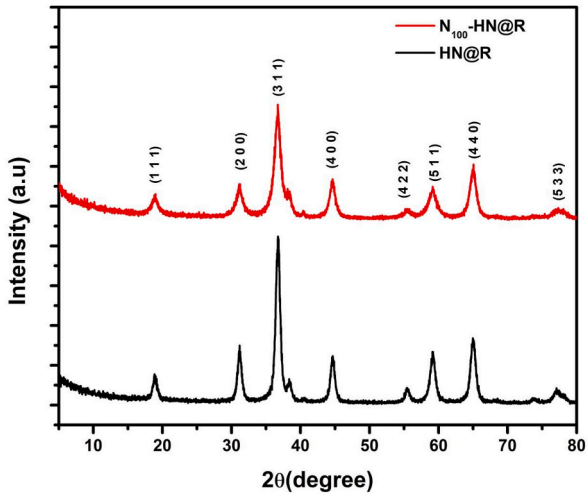

Fig. 1. XRD patterns of HN@R and N_{100}–HN@R urchin-like microspheres.

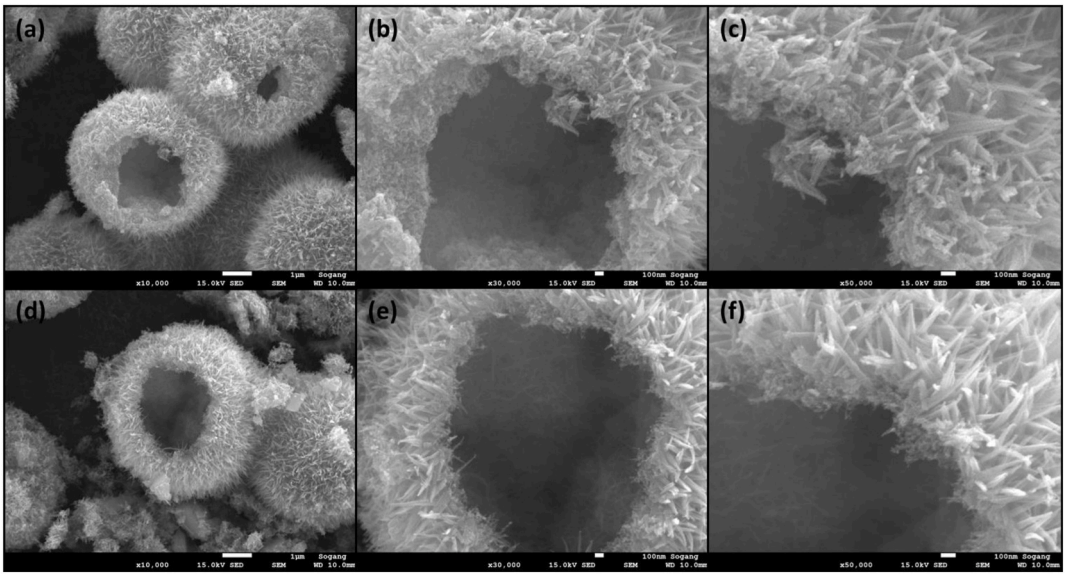

Fig. 2. FESEM images of (a–c) HN@R and (d–f) N_{100}–HN@R urchin-like microspheres at various magnifications.

amount of carbon black, were dip-coated onto an ACC substrate measuring 3 × 1 cm^2. In a typical procedure, 200 μL of a mixture containing DI water and IPA solution in a volume ratio of 3:1 was combined with 1 mg of the pseudocapacitive materials, 0.1 mg of carbon black (CB), and 10 μL of Nafion solution. The resulting solution was subjected to ultrasonication to produce a homogeneous black ink. The ACC substrate was then immersed in the ink for 60 s to allow for a substantial deposition of the materials. Afterward, it was dried at 60 °C for 10 min. This dip-dry process was repeated 5 times to achieve the desired coating thickness. Fig. S1 provides a schematic illustration of the synthesis process for the ACC/N_{100}–HN@R electrode used for glucose detection.

3. Results and discussion

3.1. Structural, surface-morphological, and porosity analysis

Fig. 1(a) illustrates the XRD patterns of the HN@R and N_{100}–HN@R microspheres. Comparing these patterns to previous research and the JCPDS 01-073-1702 database, it can be observed that both types of microspheres exhibit distinctive X-ray diffraction peaks that closely match the characteristic planes of cubic spinel $NiCo_2O_4$. It should be noted that typical diffraction peaks for RGO sheets at 25° were not observed, which could be attributed to the highly disordered structure of RGO or its low diffraction intensity [33]. The presence of sharp and distinctive key peaks in the XRD patterns indicates the well-crystallized nature of $NiCo_2O_4$, which is achieved

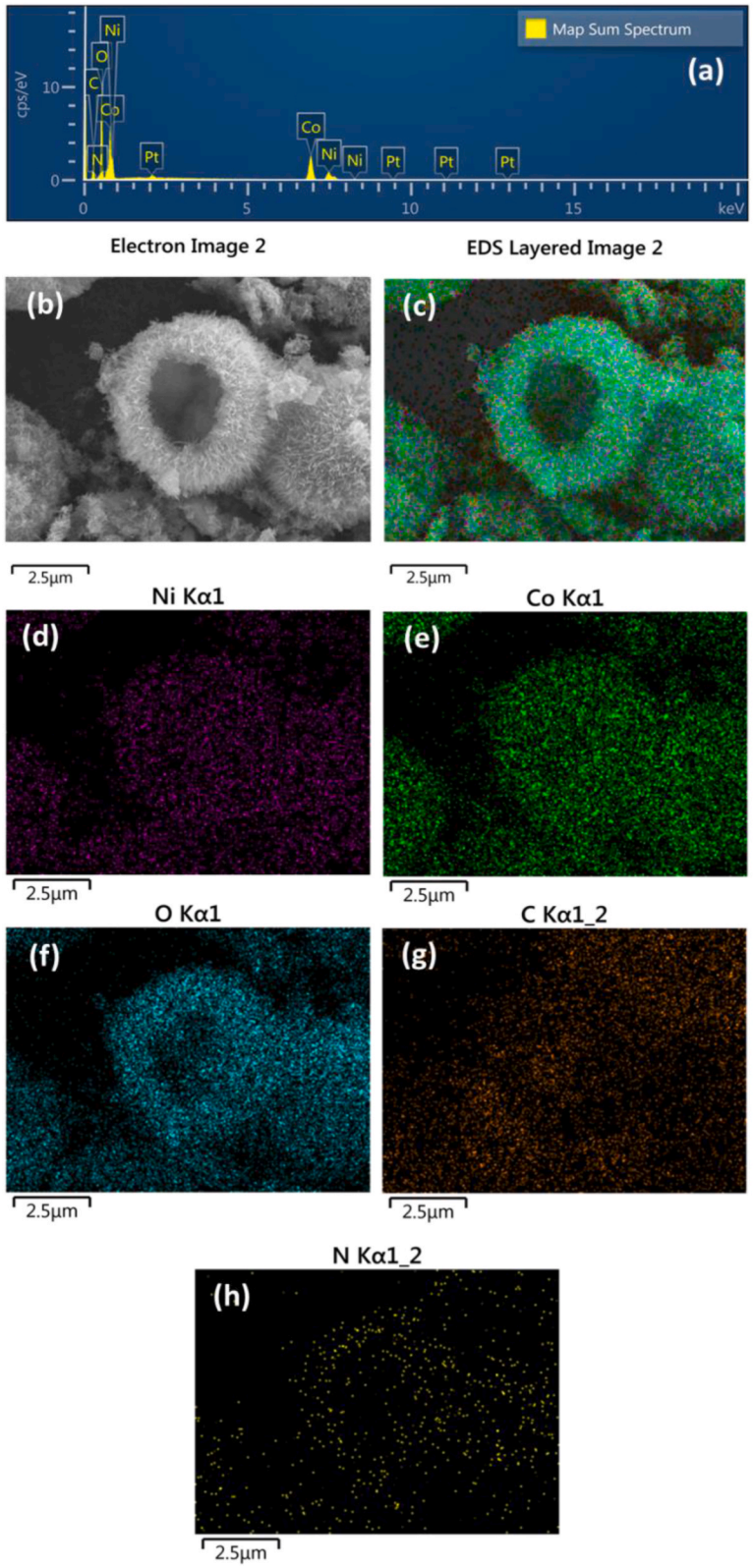

Fig. 3. (a) EDS spectrum (b) FE-SEM image, (c) EDS layer image, and the EDS mapping of (d) O (e) Co, (f) Ni, (g) C elements and (h) N N_{100}–HN@R urchin-like microspheres.

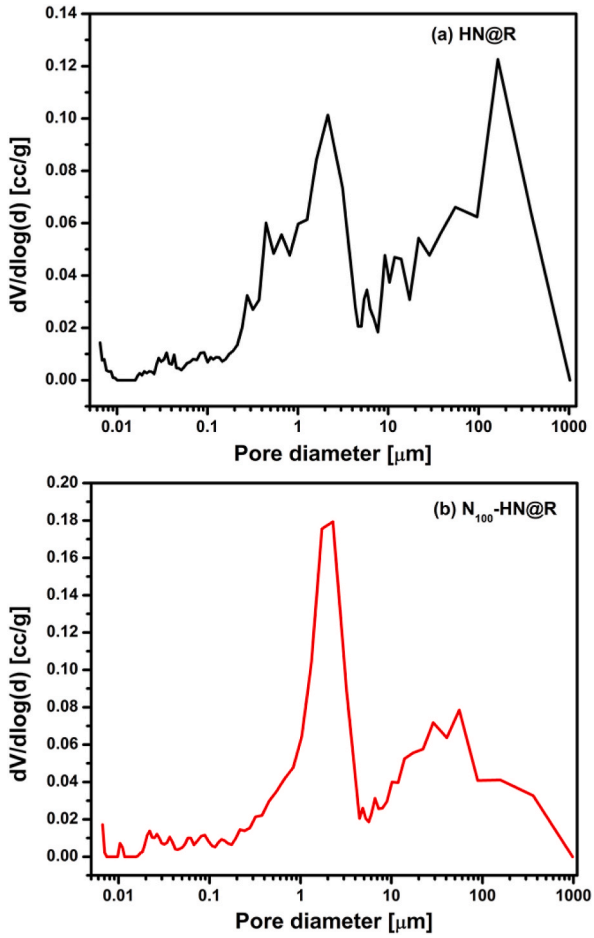

Fig. 4. Pore size distribution curves of (a) HN@R and (b) N_{100}–HN@R urchin-like microspheres.

through the controlled solvothermal reaction and thermal annealing processes. Furthermore, upon N-doping, some of the major XRD peaks for the HN@R microspheres exhibit a slight shift towards lower 2θ values. This shift can be attributed to the alteration in crystallographic characteristics resulting from the difference in ionic radii between N and O. According to Bragg's Law equation, the substitutional replacement of O by N leads to a change in the interplanar spacing (d-value) and a reduction in the diffraction angle of the (3 1 1) plane. Consequently, a slight lattice distortion is formed in the $NiCo_2O_4$ structure due to N-doping. Although the primary diffraction peak intensities are slightly reduced by N-doping, the crystallinity is only mildly affected, indicating that the overall crystalline structure remains relatively intact even after N-doping-induced lattice distortion and reorientation effects.

The average crystallite size (D) of the HN@R and N_{100}–HN@R microspheres was calculated using Scherrer's formula [34] and found to be 11 nm and 8 nm, respectively. This calculation provides an estimate of the size of the crystalline domains in the microspheres. In addition to crystallite size, the quantity of electroactive sites on the electrode material plays a crucial role in improving glucose sensing characteristics. To gain insights into the number of defects present in the microspheres, the dislocation density (δ) was assessed using the approach proposed by Williamson and Smallman [35]. The observed δ values for the HN@R and N_{100}–HN@R microspheres were 0.0077 nm and 0.0173 nm, respectively. The decrease in crystallinity, as indicated by the reduction in crystallite size, and the increase in dislocation density confirm the impact of N-doping on the microspheres. The larger defects present in the N_{100}–HN@R microspheres may contribute to their greater catalytic activity by providing more active sites for glucose sensing. Furthermore, the smaller crystallite size in the N_{100}–HN@R microspheres leads to tighter packing, increased point contacts, and improved inter-particle conductivity. These factors are expected to enhance the electrochemical processes and overall performance of the N_{100}–HN@R microspheres as a glucose-sensing material.

Fig. 2(a–f) presents FESEM images of the HN@R and N_{100}–HN@R urchin-like microspheres at various magnifications. The microspheres, with a typical diameter of approximately 5–6 μm, exhibit a hollow structure and demonstrate remarkable uniformity, as shown in Fig. 2(a, d). The formation of hollow microspheres typically involves a process known as inside-out Ostwald ripening, where the outer crystalline shells mature on solid particles and undergo continuous dissolution and re-crystallization during assembly [36, 37]. Fig. 2(b-c, e-f) provides enlarged views of these microspheres, revealing their urchin-like hierarchical structures with numerous surface-grown nanograsses. The nanograsses on the N_{100}–HN@R microspheres have a diameter of around 25 nm and a length of

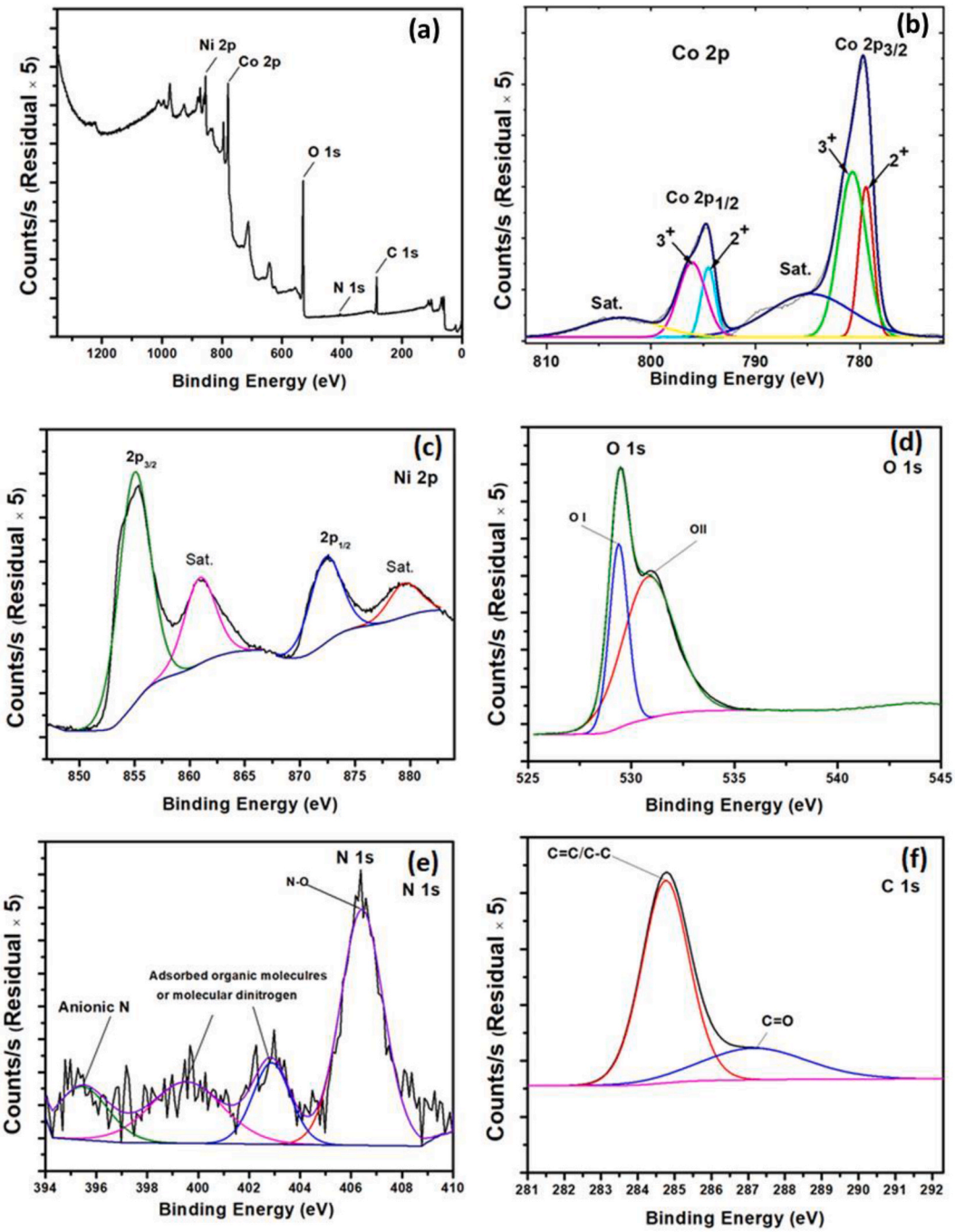

Fig. 5. (a) Survey XPS spectra, and High-resolution XPS spectra corresponding to (b) Co 2p, (c) Ni 2p, (d) O 1s, (e) N 1s, and (f) C 1s C 1s core levels of N_{100}–HN@R microspheres.

approximately 340 nm. In comparison to the N_{100}–HN@R microspheres, the interior walls of the HN@R microspheres or the roots of the nanograss appear thicker and more agglomerated. The surface nanograss structures of the N_{100}–HN@R microspheres, on the other hand, exhibit a more homogeneous and well-grown appearance. Consequently, the N_{100}–HN@R microspheres provide a significantly larger surface area with adequate porosity for electrochemical activity. Furthermore, the effective incorporation of nitrogen (N) into the spinel $NiCo_2O_4$ structure and the uniform distribution of all constituent elements, including Ni, Co, O, C, and N, were confirmed through the acquisition of the EDS spectrum and EDS mapping images of the N_{100}–HN@R microspheres, as depicted in Fig. 3(a–h). The EDS spectrum displays the relative amounts of the various elements present in the sample. Specifically, the observed weight percentages of Ni, Co, O, N, and C elements were 12.16 wt%, 24.58 wt%, 33.16 wt%, 0.56 wt%, and 29.54 wt%, respectively.

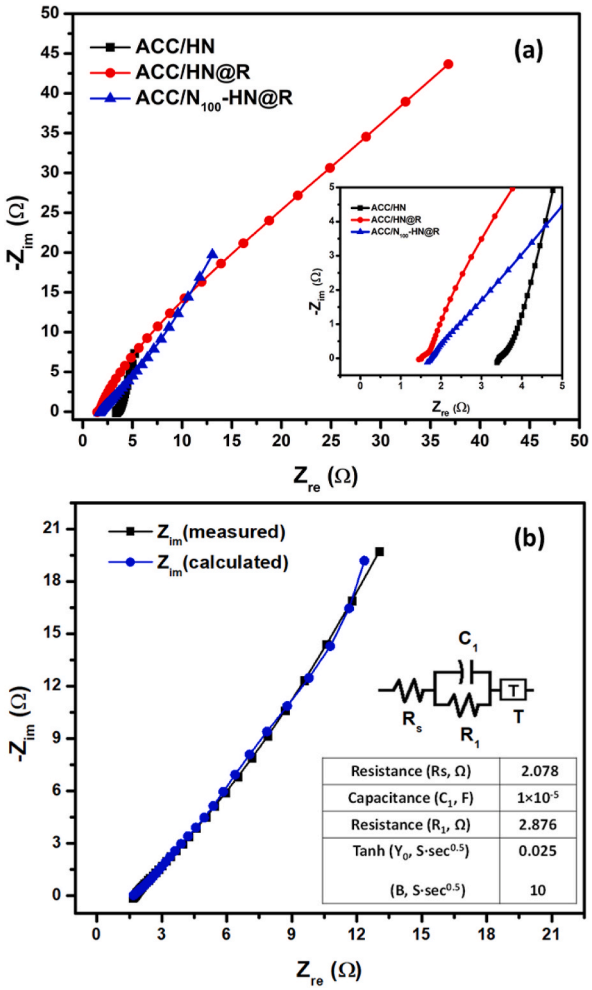

Fig. 6. (a) Electrochemical impedance spectroscopy (EIS) study (Nyquist plot) of ACC/HN, ACC/HN@R, and ACC/N_{100}–HN@R electrodes at 100 kHz–1 Hz under 0.01 V; (b) The fitted EIS plot for the ACC/N_{100}–HN@R electrode with corresponding impedance equivalent circuit. The inset table provides the values for each component of the equivalent circuit.

Additionally, to compare the N-doping concentrations and uniform distribution of constituent elements in the N_{50}–HN@R and N_{150}–HN@R microspheres, the EDS spectra and EDS mapping images of these samples were also obtained, as shown in Figs. S2 and S3, respectively. These analyses provide further evidence of the successful incorporation of N and the uniform distribution of elements in the synthesized microspheres.

In Fig. 4(a) and (b), the differential pore size distribution curves of HN@R and N_{100}–HN@R microspheres are presented. The N_{100}–HN@R microspheres exhibit significant micro- and mesoporosity, which can be attributed to their hollow structure and the presence of numerous fine nano grass-like structures on the surface, along with the uniform decoration of RGO nanoflakes. As shown in the curves, the N_{100}–HN@R microspheres demonstrate enhanced surface area and porosity compared to the HN@R microspheres. The surface area of N_{100}–HN@R microspheres is approximately 51 m^2/g, with a total porosity of 82%, whereas the HN@R microspheres exhibit a surface area of about 44 m^2/g. These porosimetry results are consistent with the FE-SEM observations and confirm the porous nature and improved surface area of the synthesized N_{100}–HN@R microspheres. The presence of a wide surface area and high porosity implies the availability of more electroactive sites, which can contribute to enhanced electrochemical activity [24]. Consequently, these properties are expected to improve the glucose-sensing capabilities of the N_{100}–HN@R microspheres.

Fig. 5(a) presents the XPS survey spectrum of the N_{100}–HN@R microspheres, providing information about the elemental composition and oxidation states on the surface. The presence of Ni, Co, O, N, and C elements in the synthesized microspheres is confirmed by the photoemission peaks' binding energies. The high-resolution XPS spectra in Fig. 5(b) show the Co 2p peaks. The peaks at 780.70 and 794.50 eV correspond to the Co^{3+} oxidation state, while the peaks at 779.42 and 794.50 eV indicate the Co^{2+} oxidation state. Additionally, the satellite peaks observed at binding energies of 796.07 and 802.80 eV are associated with Co species. The Ni 2p XPS spectra in Fig. 5(c) exhibit two peaks at binding energies of 855.28 and 872.58 eV, representing Ni $2p_{1/2}$ and Ni $2p_{3/2}$ of Ni^{2+} oxidation state, respectively. In Fig. 5(d), the O 1s XPS spectra are shown. The deconvolution of the spectrum reveals two oxygen

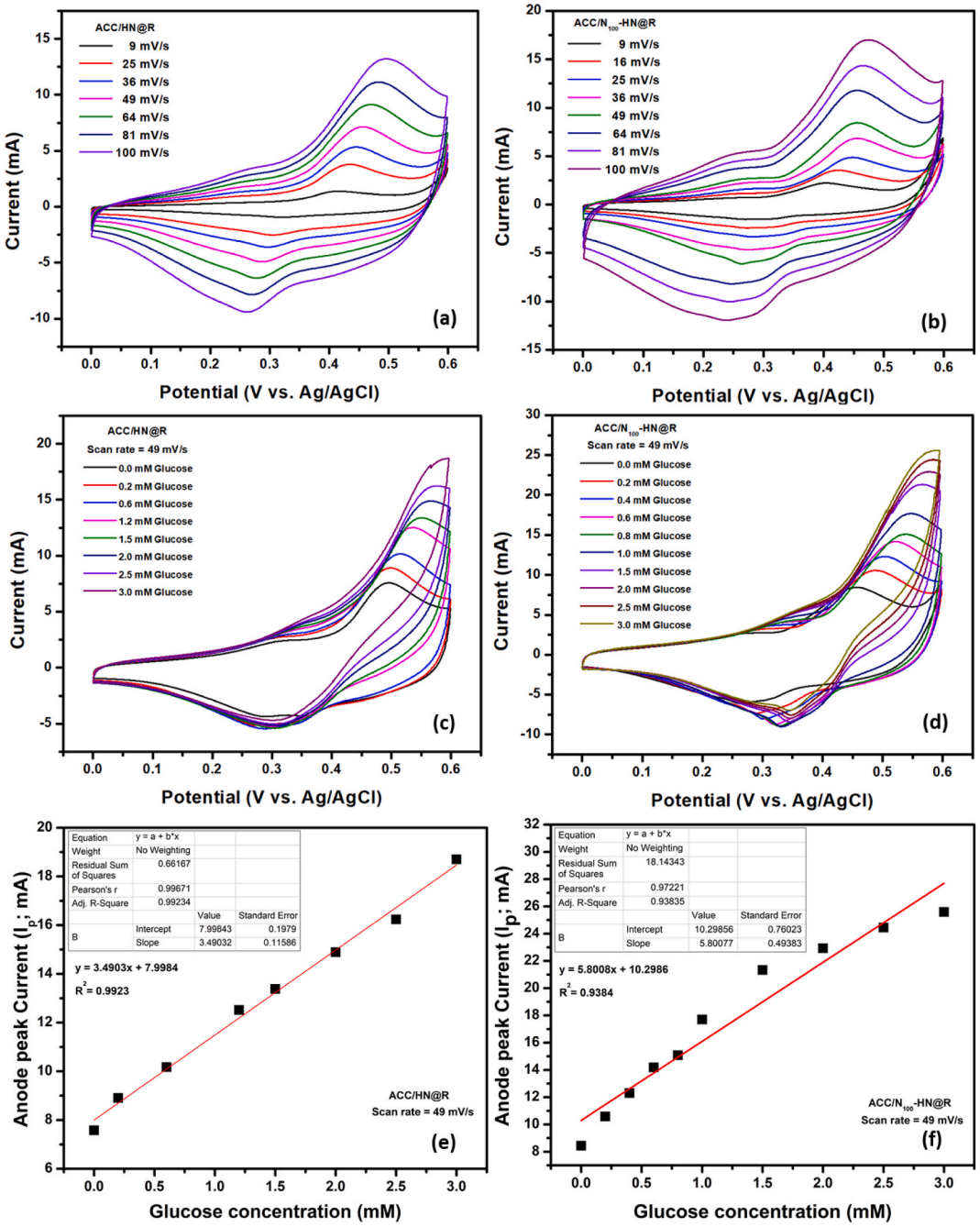

Fig. 7. Cyclic voltammetry curves of (a) ACC/HN@R, and (b) ACC/N_{100}–HN@R electrodes at various scan rates under 0 to +0.6 V potential window; Cyclic voltammetry results of glucose oxidation on (c) ACC/HN@R, and (d) ACC/N_{100}–HN@R electrodes with a glucose concentration range of 0–3 mM in 2 M KOH at 49 mV/s; the anode peak current and the glucose concentration relationship for (e) ACC/HN@R, (f) ACC/N_{100}–HN@R electrodes as obtained from cyclic voltammetry curves shown in Fig. (c) and (d), respectively.

peaks: O I at 529.38 eV, corresponding to metal-oxygen bonds, and O II at 531 eV, indicating oxygen vacancies [38]. It has been believed that the state of nitrogen is either a nitrogen anion [39] or atomic nitrogen atoms [40,41] based on XPS investigations of N_{100}–HN@R [Fig. 5(e)], which demonstrate that the N 1s core level binding energy is located at ~395 eV. Nitrogen seems to be in the state M − N (metal-nitrogen) in substituted systems, acting as an anion's substitute. However, the valence state of this substituted species is not conclusively known. While in other accounts the valence state is not specifically stated, only the presence of an M − N bond is confirmed, it has been assumed in some cases to be a N-anion. Furthermore, additional N 1s peaks at binding energies of 400 and 403 eV are observed, which can be attributed to adsorbed organic molecules or chemisorbed molecular dinitrogen. The signal

around 406 eV is associated with oxidized nitrogen [40]. The signal around 406 eV is associated with oxidized nitrogen. The deconvolution of the C 1s peaks in Fig. 5(f) reveals two main peaks at binding energies of 287.28 eV and 284.78 eV, corresponding to the C–O and C═C/C–C bonds of reduced graphene oxide (RGO), respectively.

3.2. Electrochemical properties and electrocatalytic activity of ACC/N_{100}–HN@R electrode

The EIS measurement was first performed to validate the impedance alterations during the electrode modification operations, and it was afterward utilized to examine the glucose sensing data. In Fig. 6(a), EIS measurements of ACC/HN, ACC/HN@R, and ACC/N_{100}–HN@R electrodes were performed in a 2 M KOH electrolyte over a frequency range of 1–100 kHz at 0.01 V. The Nyquist plots exhibit a small semicircle in the high-frequency region, representing the charge transfer resistance (R_{ct}) associated with faradaic processes, and a linear part in the low-frequency region, indicating capacitive behavior. The inset of Fig. 6(a) highlights that the ACC/N_{100}–HN@R electrode has the smallest semicircular diameter among the three electrodes, indicating a decrease in electron transfer resistance due to N-doping of $NiCo_2O_4$ and the presence of RGO nanoflakes on the microspheres. The initial equivalent resistance is also reduced by both N-doping and RGO decoration. Furthermore, the ACC/N_{100}–HN@R electrode exhibits a significantly shorter linear part with a steeper slope compared to the other electrodes, indicating improved electrolyte ion transport and enhanced capacitive behavior. This suggests that the synergistic effect of RGO nanoflakes and N-doping in $NiCo_2O_4$ microspheres contributes to the enhanced conductivity of the ACC/N_{100}–HN@R electrode. For comparison, Nyquist plots of ACC/N_{50}–HN@R and ACC/N_{150}–HN@R electrodes are also provided (Fig. S4), demonstrating that these electrodes exhibit lower electrochemical performance compared to the ACC/N_{100}–HN@R electrode. To gain a deeper understanding of the capacitive contributions and charge transfer mechanisms of the glucose sensor electrode, an equivalent circuit is fitted to the Nyquist plot of the ideal ACC/N_{100}–HN@R electrode, as shown in Fig. 6(b). The equivalent circuit includes an ohmic resistance (R_s) representing the combined ionic resistance of the electrolyte, interface resistance between the material and substrate, and intrinsic resistance of the current collector. The charge transfer in the surface layer of the electrode materials is characterized by the parallel connection of the R_1 and C_1 components, while the Tanh impedance, a combination of Y_0 and B, represents finite-length diffusion and blocking at the surface. The inset table of Fig. 6 (b) presents the calculated parameters corresponding to the EIS Nyquist plot, and the small amount of error indicates that the fitted model accurately represents the experimental values.

In addition to EIS, CV analysis was performed to investigate the electrochemical characteristics of the ACC/HN@R and ACC/N_{100}–HN@R electrodes in a 2 M KOH solution. Fig. 7(a) and (b) display the CV curves of the ACC/HN@R and ACC/N_{100}–HN@R electrodes, respectively, at various scan speeds within the potential range of 0 to +0.6 V. As the scan rate was increased while maintaining the non-rectangular shape of the CV curves, the integrated area under the curve and the current density also increased. The fact that the shape of the CV curves remains unchanged across all scan rates indicates excellent electrical conductivity and respectable rate capability for both electrodes. It is important to note that the current responses obtained for the ACC/N_{100}–HN@R electrode are significantly higher than those obtained for the ACC/HN@R electrode at all scan rates. Additionally, the current responses of the ACC/N_{100}–HN@R electrodes are superior to those of the ACC/HN, ACC/N_{50}–HN@R, and ACC/N_{150}–HN@R electrodes [Fig. S5 (a-c)]. This can be attributed to the enhanced porosity, nanostructure, and surface area of the ACC/N_{100}–HN@R electrode, which provides a larger number of redox-active sites, thereby improving electrochemical processes.

Both electrodes' CV curves exhibit a non-rectangular shape with two redox peaks, which characterize their pseudocapacitive behavior resulting from electrochemical reactions. These redox peaks are primarily attributed to the Faradaic reactions occurring within the electrode materials and the redox reactions taking place in the KOH electrolyte. The presence of oxygen functional groups in abundance on the RGO nanoflakes leads to strong oxidation reactions, displaying high redox reactivity in the positive potential range [42]. The corresponding electrochemical reactions are represented by Equation (1) and Equation (2) as follows:

$$NiCo_2O_4 + OH^- + H_2O \leftrightarrow NiOOH + 2CoOOH + e^- \quad (1)$$

$$CoOOH + OH^- \leftrightarrow CoO_2 + H_2O + e^- \quad (2)$$

The CV measurements were carried out at a scan rate of 49 mV/s in various concentrations of glucose (0–3 mM) added to a 0.1 M KOH electrolyte to investigate the electrocatalytic activities and mechanisms of glucose sensing on ACC/HN@R and ACC/N_{100}–HN@R electrodes [Fig. 7(c, d)]. Redox peaks corresponding to the Ni^{2+}/Ni^{3+} and Co^{2+}/Co^{3+} redox couples were observed for both electrodes, confirming the successful modification and stable deposition using the dip coating method. Noticeable increases in current response values for the anodic and cathodic peaks were observed with incremental glucose additions. The ACC/N_{100}–HN@R electrode exhibited significantly higher anodic current responses compared to the ACC/HN@R electrodes, indicating excellent electrochemical activity of the ACC/N_{100}–HN@R electrode material towards glucose. Moreover, the ACC/N_{100}–HN@R electrodes outperformed the ACC/HN, ACC/N_{50}–HN@R, and ACC/N_{150}–HN@R electrodes in terms of anodic current responses to glucose [Fig. S5 (d-f)]. The synergistic activity of Ni^{2+}, Co^{2+}, and Co^{3+} ions in the $NiCo_2O_4$ spinel structure, along with the redox couples present in $NiCo_2O_4$, serve as important active sites for glucose oxidation in alkaline media such as KOH aqueous electrolyte. The increased oxidation current of glucose on ACC/N_{100}–HN@R electrodes confirms the large electrochemically active area of N_{100}–HN@R microspheres, providing more metal ion active sites for the glucose oxidation reaction. Thus, the glucose oxidation process can be attributed to the inherent property of the spinel $NiCo_2O_4$. The electrochemical catalytic activity of $NiCo_2O_4$ for glucose oxidation [43–45] can be described as follows:

$$Co\ (IV) + Ni\ (III) + glucose \leftrightarrow Co\ (III) + Ni\ (II) + gluconolactone \quad (3)$$

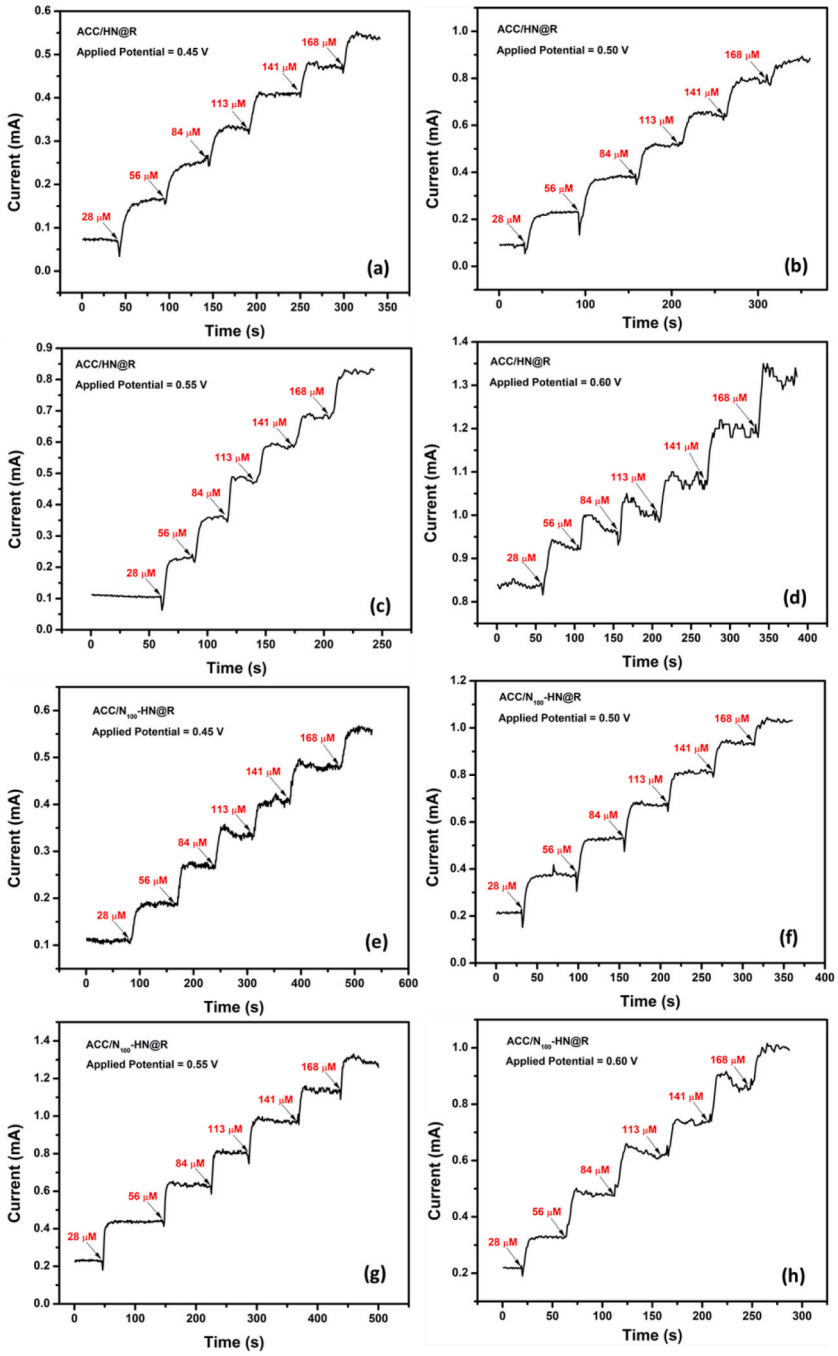

Fig. 8. The amperometric response of the electrodes (a–d) ACC/HN@R and (e–h) ACC/N_{100}–HN@R to the successive injections of 28 μM glucose into 0.1 M KOH solution at various potentials in the range of 0.40–0.60 V. (Rotation speed = 200 rpm).

The species of $NiCo_2O_4$ on the electrode surface transform NiOOH and CoOOH through an oxidation reaction during the anodic scan [equation (1)]. Subsequently, the CoOOH species is converted into CoO_2 on the electrode equation (2)]. Upon the addition of glucose to the 0.1 M KOH solution, the NiOOH and CoOOH species catalyze the oxidation of glucose, leading to the production of gluconolactone [equation (3)], which increases the oxidation current. Additionally, anodic peak potential shifts towards a positive direction with an increase in the glucose concentration, indicating electrochemical polarization between the adsorbed glucose species and the oxidized metal ion intermediates on the electrode's active sites. This phenomenon is beneficial for enhancing the oxidation of high concentrations of glucose analyte. Furthermore, Fig. 7(e, f) demonstrates the relationship between the anode peak currents and glucose concentrations, with correlation coefficients (R^2) of 0.9923 and 0.9384 for ACC/HN@R and ACC/N_{100}–HN@R electrodes,

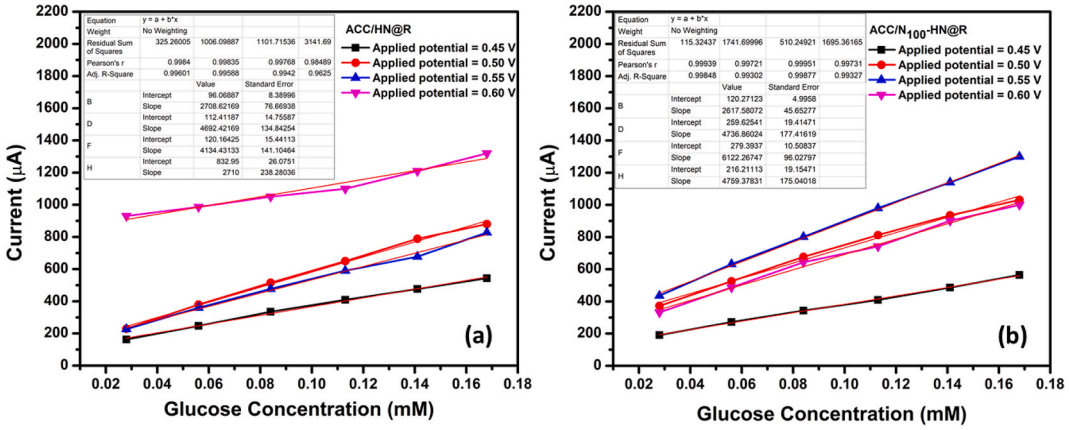

Fig. 9. Linear fit curve of glucose concentration (mM) vs. steady-state current response (μA) for (a) ACC/HN@R and ACC/N_{100}–HN@R electrodes; E_{app} = 0.40–0.60 V; Rotation speed = 200 rpm. Both plots indicate that 0.55 V is the optimum starting potential with which the electrode sensors have maximum sensitivity.

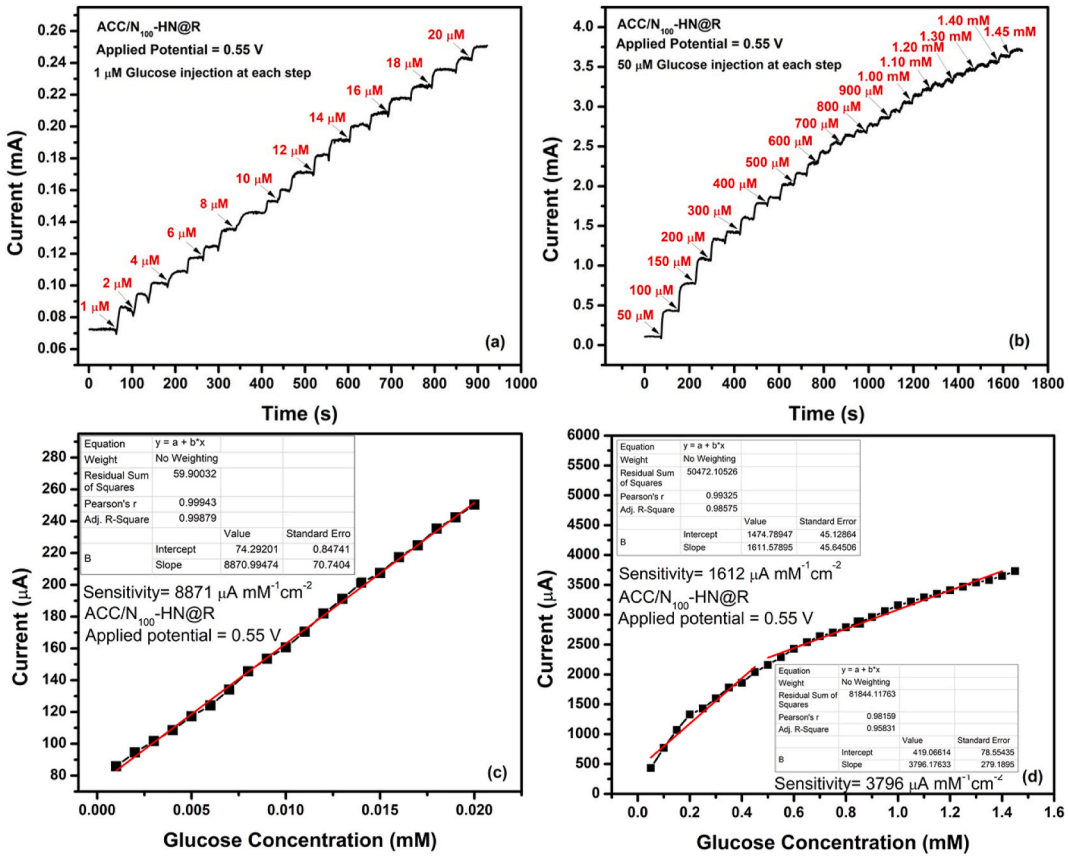

Fig. 10. (a, b) The amperometric response and respective (c, d) linear fit curves of concentration of glucose (mM) vs. steady-state current response (μA) of ACC/N_{100}–HN@R electrode sensor at E_{app} = 0.55 V for (a) low and (b) high concentration glucose injections into 0.1 M KOH solution (Rotation speed = 200 rpm).

respectively. These fitting curves exhibit a linear relationship between the response current and glucose concentration within the range of 0–3 mM. Conversely, the linear relationship between the anode peak currents and glucose concentrations for the ACC/HN, ACC/N_{50}–HN@R, and ACC/N_{150}–HN@R electrodes is relatively inadequate, as depicted in Fig. S6.

It is widely recognized that the initial potential set during amperometric measurements significantly affects the response currents

Table 1
Performance comparison of ACC/N_{100}–HN@R electrode glucose sensor with previously reported $NiCo_2O_4$ materials-based glucose sensors.

Sensor electrode	Sensitivity ($\mu M \bullet mM^{-1} \bullet cm^{-2}$)	Limit of detection (μM)	Linear range	Reference
GO-templated $NiCo_2O_4$ nanosheets	792.72	0.28	0.00015–8.86 mM	[25]
$NiCo_2O_4$/RGO hollow nanospheres	2082.57	0.7	0.04–1.28 mM	[26]
$NiCo_2O_4$ hollow nanorods	1685.1	0.16	0.0003–1.0 mM	[46]
$NiCoO_2$/C/GCE	549.3	0.5	0.02–2.41 mM	[48]
Urchin-like $NiCo_2O_4$	72.4	0.37	0.00037–2 mM	[49]
$NiCo_2O_4$ hollow nanospheres	1917	0.6	0.1–0.3 mM 0.3–2.24 mM	[50]
Graphene wrapped Co_3O_4/$NiCo_2O_4$ hollow nanocages	304	0.384	0.1–3.52 mM	[51]
$NiCo_2O_4$ nanowrinkles-RGO	38.75	38.75	0.005–8.56	[52]
ACC/$NiCo_2O_4$@RGO urchin-like microspheres	8871	0.00029	0.001–0.02 mM	This work
	6122	0.005	0.028–0.168 mM	
	3796	0.062	0.05–0.450 mM	
	1612	0.0682	0.5–1.450 mM	

[46]. Therefore, the performance of the ACC/HN@R and ACC/N_{100}–HN@R electrodes was assessed using chronoamperometric measurements following the repeated addition of glucose solution (28 μM) to the 0.1 M KOH solution. Various potentials were investigated, and the characteristic current vs. time plot was recorded while the electrolyte solution was continuously stirred at approximately 200 rpm to ensure rapid and uniform dispersion of the injected glucose solution. As observed in Fig. 8(a–h), following each injection of glucose solution within the range of 28–168 M, the oxidation currents for both electrodes exhibited an increase, resulting in staircase-like curves. An average response time of approximately 10 s was recorded. Furthermore, in comparison to the ACC/HN@R electrode, the oxidation current for the ACC/N_{100}–HN@R electrode exhibited a significant increase with the increase in glucose concentration. As shown in Fig. 8(a, e), the response currents for both electrodes were relatively low at 0.45 V. However, at a potential of 0.60 V [Fig. 8(d, h)], the noise amplitudes were considerably large, disrupting the oxidative current response and severely limiting glucose sensing capabilities [47]. Moreover, it was observed that under inappropriate potential settings, the glucose concentration had a significant impact on noise amplitudes. With successive injections of 28 μM glucose solutions, the current responses were found to be higher with minimal noise amplitudes at the initial potentials of 0.50 V and 0.55 V for both electrodes [Fig. 8(b, c, f, g)]. Fig. 8(g) demonstrates that a potential of 0.55 V results in a well-defined staircase curve with a maximum oxidation current response and excellent stability for the ACC/N_{100}–HN@R electrode. The chronoamperometric response of the ACC/N_{100}–HN@R electrode was also superior to that of the ACC/HN, ACC/N_{50}–HN@R, and ACC/N_{150}–HN@R electrodes [Fig. S7 (a-c)]. Therefore, the appropriate potential for chronoamperometric detection of glucose using an ACC/N_{100}–HN@R electrode sensor was determined to be 0.55 V. Consequently, 0.55 V was selected as the ideal starting potential for all future chronoamperometric measurements.

Fig. 9(a, b) shows the equivalent linear fit curves of the steady-state current response (A) vs. glucose concentration (mM) for the two electrodes. The observed curves produced for both electrodes at various applied potentials exhibit varied slopes (S), indicating differing sensitivity to glucose, within the examined glucose concentration range of 28–168 M. The slope values at 0.50 and 0.55 V are substantial. However, with a starting potential of 0.55 V, the ACC/N_{100}–HN@R electrode sensor has a maximum sensitivity of 6122 $\mu M\ mM^{-1}\ cm^{-2}$ ($R^2 = 0.9985$). According to the calculation, glucose has a LOD of 5 nM (S/N = 3). In comparison to the ACC/N_{100}–HN@R electrode sensor, the sensitivities calculated for the ACC/HN, ACC/N_{50}–HN@R, and ACC/N_{150}–HN@R electrodes from their linear fit curves are found to be lower [Fig. S6(d-f)]. Similar to this, chronoamperometric responses in the form of staircase-like curves were acquired corresponding to the successive additions of low and high-concentration glucose solutions into the 0.1 M KOH solution as shown in Fig. 10 (a, b) to demonstrate the broad range of glucose detection by ACC/N_{100}–HN@R electrode sensor. The resulting calibration curves for additions of low and high concentrations of glucose are shown in Fig. 10 (c, d). As can be observed, when glucose is successively injected with a step of 1 μM concentration within the range of 1–20 μM, the sensor reacts with excellent linearity and a correlation value of 0.9988. Whereas following the addition of glucose at a concentration step of 50 μM, it exhibits two distinct linear sections in the ranges of 50–450 μM and 500–1450 μM, respectively. The detection limit is therefore estimated to be 0.29 nM (S/N = 3) for the glucose concentration range of 1–20 μM, and the sensitivity of the glucose sensor is 8871 $\mu M\ mM^{-1}\ cm^{-2}$ at 0.55 V. The detection limit (82 nM) and sensitivity (1612 $\mu M\ mM^{-1}\ cm^{-2}$) were observed to be reasonable for a larger glucose concentration range i.e. 500-1450 μM.

The catalytic performance of the non-enzymatic glucose sensor was compared to previously published $NiCo_2O_4$-based glucose sensors, as shown in Table 1 [25,26,46,48–52]. The ACC/N_{100}–HN@R electrode sensor exhibited exceptional glucose-sensing ability, characterized by its remarkable sensitivity, low detection limit, and wide linear range. The sensor demonstrated a 10-s reaction time for glucose detection, which is comparable to some of the sensors mentioned in the literature. The improved intrinsic activity observed in $NiCo_2O_4$ may be attributed to enhancements in its electronic structure, evident through lattice distortion and increased electronic conductivity, which likely contribute to the enhanced sensing performance. Furthermore, the incorporation of RGO nanoflakes onto $NiCo_2O_4$ microspheres improved the material's electrical conductivity and provided additional active sites for catalytic redox processes. The highly porous hierarchical nanostructure of the sensor material, with its large effective surface area, facilitated short diffusion paths for ions or electrons and provided an abundance of electroactive sites for redox reactions, contributing to the excellent electrocatalytic sensing performance of the glucose sensor. The highly conductive ACC substrate not only served as a flexible support but also offered numerous redox-active sites and diverse channels for improved electrolyte ion transport, further enhancing the glucose sensing capability.

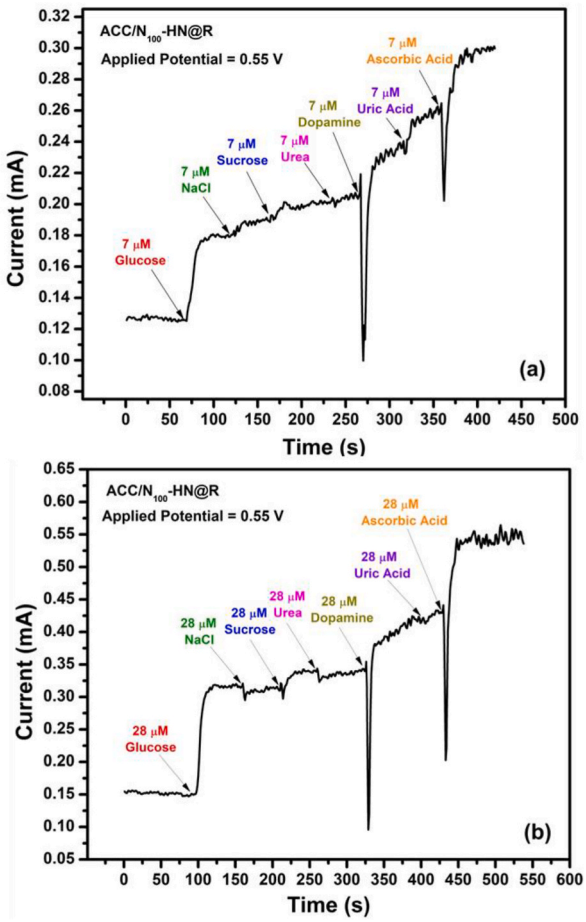

Fig. 11. Interference test of the ACC/N_{100}–HN@R electrode sensor in 0.1 M KOH with different concentrations of glucose and other interfering species as indicated.

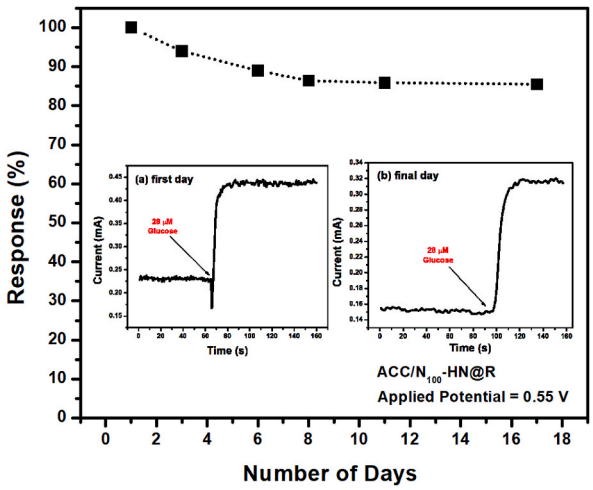

Fig. 12. Glucose sensing response stability of ACC/N_{100}–HN@R electrode sensor at E_{app} = 0.55 V for 18 days. Inset images show the first day and final day response against the 28 μM glucose injection into 0.1 M KOH solution.

One of the most critical analytical parameters for an amperometric biosensor is its ability to selectively detect and distinguish the target analyte from interfering species [37]. Human serum contains various interfering species such as urea, dopamine, ascorbic acid, NaCl, sucrose, and uric acid, which can interfere with the direct electrochemical oxidation of glucose due to their similar electrochemical processes. To assess the selectivity of the synthesized ACC/N_{100}–HN@R electrode sensor towards glucose, solutions of these interfering species were sequentially injected into the 0.1 M KOH electrolyte solution at two different concentrations: 7 and 28 M. Chronoamperometric measurements were then performed at an initial potential of 0.55 V, and the results of the interference test are presented in Fig. 11 (a, b). These results demonstrate that none of the other analyte species significantly affected the detection of glucose. Therefore, the mesoporous ACC/N_{100}–HN@R electrode sensor exhibits exclusive glucose detection in 0.1 M KOH solution, with maximum sensor response, even in the presence of interfering species commonly found in human blood.

Fig. 12 illustrates the amperometric response of the ACC/N_{100}–HN@R electrode sensor to injections of 28 M glucose in 0.1 M KOH solution for 18 days, aiming to evaluate its performance stability. The inset pictures depict the glucose-sensing responses on the first and last days. The results indicate that there is no significant decrease in response after the initial eight days, and even on the final day, the sensor still retains approximately 85% of its initial response. This demonstrates the acceptable electrochemical stability of the sensor, which can be attributed to the spinel structure of the $NiCo_2O_4$ and the mesoporous hierarchical nanostructure of the sensor material.

We conducted XRD analysis on the optimized ACC/N_{100}–HN@R electrode before and after multiple electrochemical tests (more than eight times). Fig. S8 presents the obtained results. The XRD pattern of the ACC/N_{100}–HN@R electrode shows distinct peaks corresponding to $NiCo_2O_4$, RGO, Nafion, and carbon cloth. However, after performing repeated electrochemical measurements on the electrode, the peak associated with the carbon cloth becomes more prominent, while the peaks associated with $NiCo_2O_4$, RGO, and Nafion appear to weaken. This indicates that prolonged exposure to the KOH electrolyte during the electrochemical experiments has led to some degradation of the electrode materials, particularly N_{100}–HN@R. To enhance the stability of the electrode, it is suggested to increase the number of dip-coating cycles and/or optimize the Nafion binder content in the initial ink used for the dip-coating process. These modifications may improve the electrode's durability and performance over extended periods of use.

4. Conclusions

In conclusion, we successfully developed a non-enzymatic glucose sensor by coating activated carbon cloth with hierarchically mesoporous N-doped $NiCo_2O_4$@RGO hollow microspheres using solvothermal, hydrothermal, and dip-coating methods. The introduction of N-doping in $NiCo_2O_4$ resulted in defect formation, reduced crystallite size, increased conductivity, and the creation of numerous active sites. Further N-doping facilitated the formation of well-developed and uniform hollow microspheres, leading to a significantly increased surface area with sufficient porosity for enhanced electrochemical activity. The decoration of RGO on N-doped $NiCo_2O_4$ hollow microspheres further improved conductivity and added more electroactive sites. The fabricated ACC/N_{100}–HN@R electrode exhibited excellent performance as a glucose sensor, with a maximum sensitivity of 8871 $\mu M\ mM^{-1}\ cm^{-2}$ in the glucose concentration range of 0.001–0.02 mM, a low limit of detection (LOD) of 0.29 nM, and fast response time of approximately 10 s. The sensor also demonstrated remarkable sensitivities and LODs across various high glucose concentration ranges, indicating its capability for reliable glucose detection over a wide linear range. Moreover, the stability tests revealed the promising performance of the electrode sensor over 18 days, and the selectivity tests demonstrated its ability to selectively detect glucose without significant interference from other analyte species commonly found in human serum. Overall, our findings highlight the potential of the composite material consisting of urchin-like N-doped $NiCo_2O_4$ decorated with RGO nanoflakes on activated carbon cloth as a practical solution for the development of non-enzymatic glucose sensors.

Author contribution statement

Prashant Shivaji Shewale: Conceived and designed the experiments; Performed the experiments; Analyzed and interpreted the data; Wrote the paper.

Kwang-Seok Yun: Analyzed and interpreted the data; Contributed reagents, materials, analysis tools, or data; Wrote the paper.

Data availability statement

The data that has been used is confidential.

Declaration of competing interest

The authors declare that they have no known competing financial interests or personal relationships that could have appeared to influence the work reported in this paper.

Acknowledgment

This research was supported by the Basic Science Research Program (2022R1F1A1075165) and National R&D Program (2021M3H2A1038042) through the National Research Foundation of Korea (NRF) funded by the Ministry of Science and ICT.

Appendix A. Supplementary data

Supplementary data to this article can be found online at https://doi.org/10.1016/j.heliyon.2023.e17200.

References

[1] J. Wang, Electrochemical glucose biosensors, Chem. Rev. 108 (2008) 814–825, https://doi.org/10.1021/cr068123a.
[2] X. Niu, X. Li, J. Pan, Y. He, F. Qiu, Y. Yan, Recent advances in non-enzymatic electrochemical glucose sensors based on non-precious transition metal materials: opportunities and challenges, RSC Adv. 6 (2016) 84893–84905, https://doi.org/10.1039/C6RA12506A.
[3] K. Qu, S. Wang, W. He, H. Yin, L. Wang, Y. Zheng, Ternary metal oxide nanorods ($Ni_{0.5}Cu_{0.5}Co_2O_4$) as efficient positive materials for non-enzymatic glucose sensing and fuel cell application, Solid State Sci. 135 (2023), 107070, https://doi.org/10.1016/j.solidstatesciences.2022.107070.
[4] Z. Zhang, H. Yin, H. Zhao, L. Wang, J. Gong, Q. Nie, S. Wu, Deposition of platinum on MOF derived NiS_x/NCNTs for highly efficient glucose oxidation, Inorg. Chem. Commun. 144 (2022), 109887, https://doi.org/10.1016/j.inoche.2022.109887.
[5] J. Chen, H. Yin, J. Zhou, L. Wang, J. Gong, Z. Ji, Q. Nie, Efficient nonenzymatic sensors based on Ni-MOF microspheres decorated with Au nanoparticles for glucose detection, J. Electron. Mater. 49 (2020) 4754–4763, https://doi.org/10.1007/s11664-020-08191-x.
[6] J. Zhou, H. Yin, J. Chen, J. Gong, L. Wang, Y. Zheng, Q. Nie, Electrodeposition of bimetallic NiAu alloy dendrites on carbon papers as highly sensitive disposable non-enzymatic glucose sensors, Mater. Lett. 273 (2020), 127912, https://doi.org/10.1016/j.matlet.2020.127912.
[7] M. Ezzati, S. Shahrokhian, H. Hosseini, In situ two-step preparation of 3D NiCo-BTC MOFs on a glassy carbon electrode and a graphitic screen printed electrode as nonenzymatic glucose-sensing platforms, ACS Sustainable Chem. Eng. 8 (38) (2020) 14340–14352, https://doi.org/10.1021/acssuschemeng.0c03806.
[8] S. Shahrokhian, M. Ezzati, H. Hosseini, Fabrication of a sensitive and fast response electrochemical glucose sensing platform based on Co-based metal-organic frameworks obtained from rapid in situ conversion of electrodeposited cobalt hydroxide intermediates, Talanta 210 (2020), 120696, https://doi.org/10.1016/j.talanta.2019.120696.
[9] S. Shahrokhian, E.K. Sanati, H. Hosseini, Direct growth of metal-organic frameworks thin film arrays on glassy carbon electrode based on rapid conversion step mediated by copper clusters and hydroxide nanotubes for fabrication of a high-performance non-enzymatic glucose sensing platform, Biosens. Bioelectron. 112 (2018) 100–107, https://doi.org/10.1016/j.bios.2018.04.039.
[10] H. Hosseini, H. Ahmar, A. Dehghani, A. Bagheri, A. Tadjarodi, A. Fakhari, A novel electrochemical sensor based on the metal-organic framework for electrocatalytic oxidation of L-cysteine, Biosens. Bioelectron. 42 (2013) 426–429, https://doi.org/10.1016/j.bios.2012.09.062.
[11] F. Zhou, Q. Wang, K. Huang, X. Jiang, Z. Zou, X. Xiong, Flame synthesis of NiO nanoparticles on carbon cloth: an efficient non-enzymatic sensor for glucose and formaldehyde, Microchem. J. 159 (2020), 105505, https://doi.org/10.1016/j.microc.2020.105505.
[12] Z. Cui, H. Yin, Q. Nie, D. Qin, W. Wu, X. He, Hierarchical flower-like NiO hollow microspheres for non-enzymatic glucose sensors, J. Electroanal. Chem. 757 (2015) 51–57, https://doi.org/10.1016/j.jelechem.2015.09.011.
[13] H. Shu, S. Peng, T. Lai, X. Cui, J. Ren, T. Chen, X. Xiao, Y. Wang, Nickel foam electrode decorated with Fe-$CdIn_2O_4$ nanoparticles as an effective electrochemical sensor for non-enzymatic glucose detection, J. Electroanal. Chem. 919 (2022), 116524, https://doi.org/10.1016/j.jelechem.2022.116524.
[14] L. Yang, J. Yang, Q. Dong, F. Zhou, Q. Wang, Z. Wang, K. Huang, H. Yu, X. Xiong, One-step synthesis of CuO nanoparticles based on flame synthesis: as a highly effective non-enzymatic sensor for glucose, hydrogen peroxide, and formaldehyde, J. Electroanal. Chem. 881 (2021), 114965, https://doi.org/10.1016/j.jelechem.2020.114965.
[15] P. Yang, X. Wang, C.-Y. Ge, X. Fu, X.Y. Liu, H. Chai, X. Guo, H.-C. Yao, Y.X. Zhang, K. Chen, Fabrication of CuO nanosheets-built microtubes via Kirkendall effect for a non-enzymatic glucose sensor, Appl. Surf. Sci. 494 (2019) 484–491, https://doi.org/10.1016/j.apsusc.2019.07.197.
[16] X. Lin, Y. Wang, M. Zou, T. Lan, Y. Ni, Electrochemical non-enzymatic glucose sensors based on nano-composite of Co_3O_4 and multiwalled carbon nanotube, Chin. Chem. Lett. 30 (2019) 1157–1160, https://doi.org/10.1016/j.cclet.2019.04.009.
[17] Z. Gao, L. Zhang, C. Ma, Qi Zhou, Y. Tang, Z. Tu, W. Yang, L. Cui, Y. Li, TiO_2 decorated Co_3O_4 acicular nanotube arrays and its application as a non-enzymatic glucose sensor, Biosens. Bioelectron. 80 (2016) 511–518, https://doi.org/10.1016/j.bios.2016.02.004.
[18] J. Chen, W.-D. Zhang, J.-S. Ye, Nonenzymatic electrochemical glucose sensor based on MnO_2/MWNTs nanocomposite, Electrochem. Commun. 10 (2008) 1268–1271, https://doi.org/10.1016/j.elecom.2008.06.022.
[19] Y. Wang, W. Bai, F. Nie, J. Zheng, A non-enzymatic glucose sensor based on Ni/MnO_2 nanocomposite modified glassy carbon electrode, Electroanalysis 27 (2015) 2399–2405, https://doi.org/10.1002/elan.201500049.
[20] L.-Y. Lin, B.B. Karakocak, S. Kavadiya, T. Soundappan, P. Biswas, A highly sensitive non-enzymatic glucose sensor based on Cu/Cu_2O/CuO ternary composite hollow spheres prepared in a furnace aerosol reactor, Sens. Actuators, B 259 (2018) 745–752, https://doi.org/10.1016/j.snb.2017.12.035.
[21] R. Manafi-Yeldaghermani, S. Shahrokhian, M.H. Kahnamouei, Facile preparation of a highly sensitive non-enzymatic glucose sensor based on the composite of $Cu(OH)_2$ nanotubes arrays and conductive polypyrrole, Microchem. J. 169 (2021), 106636, https://doi.org/10.1016/j.microc.2021.106636.
[22] L. Liu, Z. Wang, J. Yang, G. Liu, J. Li, L. Guo, S. Chen, Q. Guo, $NiCo_2O_4$ nanoneedle decorated electrospun carbon nanofiber nanohybrids for sensitive non-enzymatic glucose sensors, Sens. Actuators, B 258 (2018) 920–928, https://doi.org/10.1016/j.snb.2017.11.118.
[23] S. Wang, L. Li, W. He, Y. Shao, Y. Li, Y. Wu, X. Hao, Oxygen vacancy modulation of bimetallic oxynitride anodes toward advanced Li-ion capacitors, Adv. Funct. Mater. 30 (27) (2020), 2000350, https://doi.org/10.1002/adfm.202000350.
[24] X.-Y. Yu, X.-Z. Yao, T. Luo, Y. Jia, J.-H. Liu, X.-J. Huang, Facile synthesis of urchin-like $NiCo_2O_4$ hollow microspheres with enhanced electrochemical properties in energy and environmentally related applications, ACS Appl. Mater. Interfaces 6 (2014) 3689–3695, https://doi.org/10.1021/am4060707.
[25] S.M. Babulal, S.-M. Chen, R. Palani, K. Venkatesh, A.S. Haidyrah, S.K. Ramaraj, C.-C. Yang, C. Karuppiah, Graphene oxide template based synthesis of $NiCo_2O_4$ nanosheets for high-performance non-enzymatic glucose sensor, Colloids Surf., A 621 (2021), 126600, https://doi.org/10.1016/j.colsurfa.2021.126600.
[26] B. Wang, Y. Cao, Y. Chen, X. Lai, J. Peng, J. Tu, X. Li, Rapid synthesis of rGO conjugated hierarchical $NiCo_2O_4$ hollow mesoporous nanospheres with enhanced glucose sensitivity, Nanotechnology 28 (2017), 025501, https://doi.org/10.1088/0957-4484/28/2/025501.
[27] K. Choi, I.K. Moon, J. Oh, An efficient amplification strategy for N-doped $NiCo_2O_4$ with oxygen vacancies and partial Ni/Co-nitrides as a dual-function electrode for both supercapatteries and hydrogen electrocatalysis, J. Mater. Chem. 7 (2019) 1468–1478, https://doi.org/10.1039/c8ta07210h.
[28] S. Liu, Y. Yin, D. Ni, K.S. Hui, K.N. Hui, S. Lee, C.-Y. Ouyang, S.C. Jun, Phosphorous-containing oxygen-deficient cobalt molybdate as an advanced electrode material for supercapacitors, Energy Storage Mater. 19 (2019) 186–196, https://doi.org/10.1016/j.ensm.2018.10.022.
[29] Y. Zeng, Z. Lai, Y.i. Han, H. Zhang, S. Xie, X. Lu, Oxygen-vacancy and surface modulation of ultrathin nickel cobaltite nanosheets as a high-energy cathode for advanced Zn-ion batteries, Adv. Mater. 30 (2018), 1802396, https://doi.org/10.1002/adma.201802396.
[30] T. Zhai, L. Wan, S. Sun, Q. Chen, J. Sun, Q. Xia, H. Xia, Phosphate ion functionalized Co_3O_4 ultrathin nanosheets with greatly improved surface reactivity for high-performance pseudocapacitors, Adv. Mater. 29 (7) (2017), 1604167, https://doi.org/10.1002/adma.201604167.
[31] Y. Zhang, L.i. Tao, C. Xie, D. Wang, Y. Zou, R.u. Chen, Y. Wang, C. Jia, S. Wang, Defect engineering on electrode materials for rechargeable batteries, Adv. Mater. 32 (2020), 1905923, https://doi.org/10.1002/adma.201905923.
[32] J. Bian, X. Cheng, X. Meng, J. Wang, J. Zhou, S. Li, Y. Zhang, C. Sun, Nitrogen-doped $NiCo_2O_4$ microsphere as an efficient catalyst for flexible rechargeable Zinc−Air batteries and self-charging power system, ACS Appl. Energy Mater. 2 (2019) 2296–2304, https://doi.org/10.1021/acsaem.9b00120.
[33] J. Qi, Y. Chang, Y. Sui, Y. He, Q. Meng, F. Wei, Y. Ren, Y. Jin, Facile synthesis of Ag-decorated Ni_3S_2 nanosheets with 3D bush structure grown on rGO and its application as positive electrode material in asymmetric supercapacitor, Adv. Mater. Interfac. 5 (2018), 1700985, https://doi.org/10.1002/admi.201700985.

[34] J. Langford, A. Wilson, Scherrer after sixty years: a survey and some new results in the determination of crystallite size, J. Appl. Crystallogr. 11 (1978) 102–103, https://doi.org/10.1107/S0021889878012844.
[35] W. Xu, J. Chen, M. Yu, Y. Zeng, Y. Long, X. Lu, Y. Tong, Sulphur-doped Co_3O_4 nanowires as an advanced negative electrode for high-energy asymmetric supercapacitors, J. Mater. Chem. 4 (2016) 10779–10785, https://doi.org/10.1039/c6ta03153f.
[36] X.W. Lou, Y. Wang, C.L. Yuan, J.Y. Lee, L.A. Archer, Template-free synthesis of SnO_2 hollow nanostructures with high lithium storage capacity, Adv. Mater. 18 (2006) 2325–2329, https://doi.org/10.1002/adma.200600733.
[37] A.Q. Pan, H.B. Wu, L. Yu, X.W. Lou, Template-free synthesis of VO_2 hollow microspheres with various interiors and their conversion into V_2O_5 for lithium-ion batteries, Angew. Chem., Int. Ed. 52 (2013) 2226–2230, https://doi.org/10.1002/anie.201209535.
[38] L. Hou, W. Yang, X. Xu, B. Deng, J. Tian, S. Wang, F. Yang, Y. Li, In-situ formation of oxygen-vacancy-rich NiCo2O4/nitrogen-deficient graphitic carbon nitride hybrids for high-performance supercapacitors, Electrochim. Acta 340 (2020), 135996, https://doi.org/10.1016/j.electacta.2020.135996.
[39] R. Asahi, T. Morikawa, T. Ohwaki, K. Aoki, Y. Taga, Visible-light photocatalysis in nitrogen-doped titanium oxides, Science 293 (2001) 269–271.
[40] T. Sano, N. Negishi, K. Koike, K. Takeuchi, S. Matsuzawa, Preparation of a visible light-responsive photocatalyst from a complex of Ti4+ with a nitrogen-containing ligand, J. Mater. Chem. 14 (2004) 380–384.
[41] O. Diwald, T.L. Thompson, T. Zubkov, E.G. Goralski, S.D. Walck, J.T. Yates, Photochemical activity of nitrogen-doped rutile TiO2(110) in visible light, J. Phys. Chem. B 108 (2004) 6004–6008.
[42] C. Zhao, Q. Wang, H. Zhang, S. Passerini, X. Qian, Two-dimensional titanium carbide/rgo composite for high-performance supercapacitors, ACS Appl. Mater. Interfaces 8 (2016) 15661–15667, https://doi.org/10.1021/acsami.6b04767.
[43] Y. Ding, Y. Wang, L. Su, M. Bellagamba, H. Zhang, Y. Lei, Electrospun Co_3O_4 nanofibers for sensitive and selective glucose detection, Biosens. Bioelectron. 26 (2010) 542–548, https://doi.org/10.1016/j.bios.2010.07.050.
[44] R. Ding, L. Qi, M. Jia, H. Wang, Simple hydrothermal synthesis of mesoporous spinel $NiCo_2O_4$ nanoparticles and their catalytic behavior in CH_3OH electro-oxidation and H_2O_2 electro-reduction, Catal. Sci. Technol. 3 (2013) 3207–3215, https://doi.org/10.1039/C3CY00590A.
[45] W.D. Zhang, J. Chen, L.C. Jiang, Y.X. Yu, J.Q. Zhang, A highly sensitive nonenzymatic glucose sensor based on NiO-modified multi-walled carbon nanotubes, Microchim. Acta 168 (2010) 259–265, https://doi.org/10.1007/s00604-010-0288-2.
[46] J. Yang, M. Cho, Y. Lee, Synthesis of hierarchical $NiCo_2O_4$ hollow nanorods via sacrificial-template accelerate hydrolysis for electrochemical glucose oxidation, Biosens. Bioelectron. 75 (2016) 15–22, https://doi.org/10.1016/j.bios.2015.08.008.
[47] Y. Zhang, D. Zhao, W. Zhu, W. Zhang, Z. Yue, J. Wang, R. Wang, D. Zhang, J. Wang, G. Zhang, Engineering multi-stage nickel oxide rod-on-sheet nanoarrays on Ni foam: a superior catalytic electrode for ultrahigh-performance electrochemical sensing of glucose, Sensor. Actuator. B 255 (2018) 416–423, https://doi.org/10.1016/j.snb.2017.08.078.
[48] X. Tang, B. Zhang, C. Xiao, H. Zhou, X. Wang, D. He, Carbon nanotube template synthesis of hierarchical $NiCoO_2$ composite for non-enzyme glucose detection, Sens. Actuators, B 222 (2016) 232–239, https://doi.org/10.1016/j.snb.2015.08.077.
[49] Z. Qin, Q. Cheng, Y. Lu, J. Li, Facile synthesis of hierarchically mesoporous $NiCo_2O_4$ nanowires for sensitive non-enzymatic glucose detection, Appl. Phys. A 123 (2017) 492, https://doi.org/10.1007/s00339-017-1108-x.
[50] W. Huang, Y. Cao, Y. Chen, J. Peng, X. Lai, J. Tu, Fast synthesis of porous $NiCo_2O_4$ hollow nanospheres for a high-sensitivity non-enzymatic glucose sensor, Appl. Surf. Sci. 396 (2017) 804–811, https://doi.org/10.1016/j.apsusc.2016.11.034.
[51] B. Xue, K. Li, L. Feng, J. Lu, L. Zhang, Graphene wrapped porous Co_3O_4/$NiCo_2O_4$ double-shelled nanocages with enhanced electrocatalytic performance for glucose sensor, Electrochim. Acta 239 (2017) 36–44, https://doi.org/10.1016/j.electacta.2017.04.005.
[52] G. Ma, M. Yang, C. Li, H. Tan, L. Deng, S. Xie, F. Xu, L. Wang, Y. Song, Preparation of spinel nickel-cobalt oxide nanowrinkles/reduced graphene oxide hybrid for nonenzymatic glucose detection at physiological level, Electrochim. Acta 220 (2016) 545–553, https://doi.org/10.1016/j.electacta.2016.10.163.

Prashant Shivaji Shewale graduated from Shivaji University, Kolhapur, India, with a B·Sc. in Physics in 2006, an M.S. in Physics in 2008, and a Ph.D. in Physics in 2013. In Busan, South Korea's Dong-Eui University, he worked as a post-doctoral researcher from 2013 to 2018. He began working as a research professor in the Department of electronic engineering at Sogang University in Seoul, Korea, in January 2019. He has so far published 25 articles in international journals as well as one book. His current research focuses on energy storage/conversion devices, electrochemical sensors, UV photodetectors, low-temperature nanocomposite-based gas sensors, MEMS, and integrated systems.

Kwang-Seok Yun graduated with a B.S. in Electronics Engineering from Kyungpook National University in 1996, an M.S. in Electrical Engineering from Korea Advanced Institute of Science and Technology (KAIST) in 1997, and a Ph.D. in Electrical Engineering from the same institution in 2002. From 2005 to 2007, he worked as a postdoctoral researcher at the University of California, Los Angeles. In March 2007, he began teaching in the Department of Electronic Engineering at Sogang University in Seoul, Korea, where he is presently a Professor. Micro transducers, sensors, actuators, MEMS, as well as signal/energy storage/conversion devices, circuits, and systems, are among his current research interests.